https://doi.org/10.1016/j.jfluidstructs.2019.02.006

On the aeroelastic energy transfer from a Lamb dipole to a flexible cantilever

Chenglei Wang, Hui Tang*

Department of Mechanical Engineering, The Hong Kong Polytechnic University, Kowloon, Hong Kong SAR, China

Abstract

This paper studies the aeroelastic energy transfer from an advecting Lamb dipole to a flexible cantilever. The cantilever is initially placed either along or against the dipole's advection direction with various lateral distances. As the dipole moves towards the cantilever, they interact and exchange the energy. Such a fluid-structure interaction problem is numerically solved at a low Reynolds number of 200 using a lattice Boltzmann method based numerical framework. The simulation results confirm that, when the lateral distance is around the dipole radius, placing the cantilever against the dipole's advection direction is more favorable for energy transfer. Under this setting, the cantilever generally experiences two notable increases in its mechanical energy. The first one is caused by the direct impact associated with the dipole's approach, whereas the second one occurs when the dipole just passes by and exerts suction on the cantilever's free end. Each increase leads to a peak, and the second peak is much larger representing the maximum transferred energy. It is further found that when the lateral distance is about a half of the dipole radius, the cantilever's length is about one dipole radius, and its bending stiffness is moderate, the aeroelastic efficiency can be as high as 10.6%.

Keywords: Fluid-structure interaction, Energy transfer, Vortex dynamics, Lamb dipole

*Corresponding author
Email address: `h.tang@polyu.edu.hk` (Hui Tang)

Preprint submitted to Journal of Fluids and Structures *January 2, 2019*

1. Introduction

Small-scale energy harvesting is gaining considerable attentions due to increasing desires for self-powered miniature electronic devices used in various applications, such as structural health monitoring [1], aquatic tracking systems [2], and medical implants [3], just to name a few. One of the most popular and effective ways is scavenging energy through interactions of elastic structures with surrounding flows, in which two types of electromechanical transducers, also known as smart materials, are commonly used [4]. The first type, such as piezoelectric transducers, shows strong electromechanical coupling, in which the structural deformation can cause electric displacement and the electric field can also induce stresses in structures. The second type, such as ionic polymer metal composite (IPMC), only exhibits weak electromechanical coupling.

With either type of smart materials being deployed, harvesters are able to convert mechanical energy into electrical energy when they interact with surrounding flows and deform. Specifically, this fluidic energy harvesting process is usually completed through three major steps [4, 5, 6]. First, the fluid kinetic energy is transferred to the harvester in the form of mechanical energy. Second, the mechanical energy is converted into electric energy using a suitable electric generator. Finally, the electric energy is conditioned and converted into chemical/electrical energy that can be stored in rechargeable batteries/capacitors. The corresponding energy conversion efficiencies in these three steps are termed as the "aeroelastic efficiency", the "electromechanical efficiency" and the "electrical conditioning efficiency", respectively, the multiplication of which gives the total energy harvesting efficiency.

The first step of the fluidic energy harvesting involves typical fluid-structure interactions (FSI), and it has been extensively investigated in various modalities involving the use of aeroelastic instabilities [7], flapping flags [8], wakes downstream of bluff bodies [9], and single and multiple flexible filaments [10]. On these topics, Priya and Inman [3], Elvin and Erturk [4], and Erturk and

Inman [11] have given comprehensive reviews. Recently, another modality has received special attentions, i.e., energy transfer through FSI from coherent flow structures to deformable cantilevers [6, 12, 13, 14, 15, 16]. The coherent flow structures are often modeled as vortex rings/pairs/dipoles due to their ubiquity in nature, and the cantilevers are usually placed either against or perpendicular to the vortex advection direction. For example, Peterson and Porfiri [6] experimentally studied the energy harvesting of an IPMC beam perpendicularly interacting with a convecting vortex ring. They observed that the aeroelastic efficiency varied in the range from 0.5% to 1.5%. Without considering the damping effects, Zivkov *et al.* [14] conducted two-dimensional numerical simulations on a similar problem, but replaced the vortex ring by a Lamb dipole and assumed that the cantilever exhibited weak electromechanical coupling. They found that the aeroelastic efficiency was up to 5%. They also observed that when the Lamb dipole impinged on the cantilever, secondary dipoles appeared and may exert additional impacts on the cantilever thus transfer more energy. These findings were further confirmed by their recent experimental study [15].

A few studies also focused on cantilevers placed against advecting coherent vortex structures. For example, Goushcha *et al.*[12] experimentally demonstrated the capability of a single piezoelectric cantilever in scavenging energy from one or multiple vortex rings. This work was then followed up by Hu *et al.*[13], in which a theoretical model was established. To develop the model, they proposed a ring-to-pair conversion scheme and casted the three-dimensional problem into a two-dimensional framework. Moreover, they assumed that the fluid was inviscid, the cantilever obeyed the Kirchhoff-Love plate theory, and the lateral distance between the vortex and the cantilever was sufficiently large to avoid discernible interactions. Although useful, these assumptions and simplifications limit the applicability of this model. To overcome this, the same group [16] further incorporated viscous and three-dimensional effects into their model. However, this upgraded model was not able to faithfully resolve the strong interaction between the vortex and the cantilever occurring in their experimental case with the distance ratio of 1.37, where the maximum aeroelastic

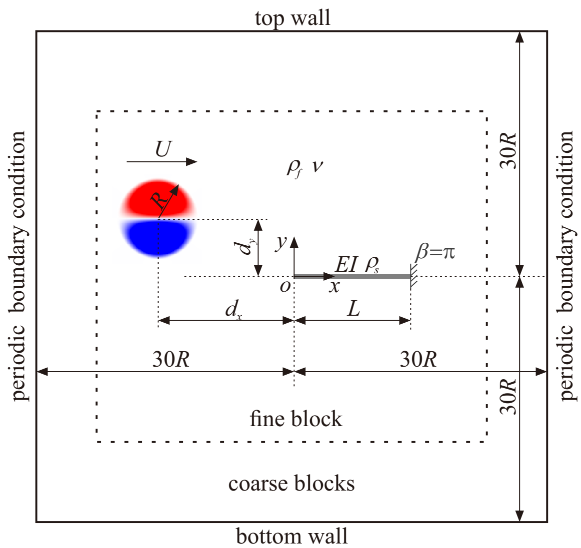

Figure 1: Schematic of a Lamb dipole moving against a flexible cantilever, and the computational domain (not in scale) with implemented boundary conditions used in the present study.

efficiency of around 0.82% was achieved.

Although interactions of coherent flow structures with flexible cantilevers and the resulting energy transfer have been investigated using different configurations as introduced above, the effects of several key parameters were seldom explored especially under strong interactions, such as the cantilever's orientation, bending stiffness, length and vertical distance from the coherent flow structure. Aiming at filling this gap so as to further extend our understanding in the energy transfer from coherent flow structures to deformable structures, in this paper we study the effects of these key parameters through a detailed examination of the strong FSI between a Lamb dipole advecting along/against a flexible cantilever.

2. Problem description and methodology

2.1. Problem description

In this study, energy transfer from a vortex dipole to a thin flexible cantilever in an incompressible flow of density ρ_f and kinematic viscosity ν is numerically investigated in a two-dimensional domain. The schematic at the start of the simulation, i.e., $t = 0$, is sketched in Figure 1. The vortex dipole is modeled as a Lamb dipole with radius R and horizontal advection velocity U. Downstream of the dipole is placed a horizontal, initially undeformed cantilever with length L, bending stiffness EI, and linear density ρ_s. The cantilever is clamped at its one end and free at the other. Its orientation angle is defined as $\beta = 0$ if its left end is clamped, and $\beta = \pi$ otherwise. For illustration purpose the configuration with $\beta = \pi$ is shown in Figure 1. The initial horizontal and vertical distances of the cantilever's left end from the dipole center are defined as d_x and d_y, respectively.

In this study, the clamped-free cantilever is assumed as an inextensible, purely elastic plate exhibiting weak electromechanical coupling behavior [4]. As such, its dynamics is governed by two nonlinear structure equations [17]

$$\rho_s \frac{\partial^2 \boldsymbol{X}}{\partial t^2} - \frac{\partial}{\partial s}\left(T\frac{\partial \boldsymbol{X}}{\partial s}\right) + \frac{\partial^2}{\partial s^2}\left(EI\frac{\partial^2 \boldsymbol{X}}{\partial s^2}\right) = \boldsymbol{F}_f \tag{1}$$

$$\frac{\partial \boldsymbol{X}}{\partial s}\cdot\frac{\partial \boldsymbol{X}}{\partial s} = 1 \tag{2}$$

with boundary conditions

$$y = 0;\ \frac{\partial \boldsymbol{X}}{\partial s} = (\cos\beta, \sin\beta) \qquad \text{imposed at the clamped end,}$$

$$\text{and} \qquad T = 0;\ \frac{\partial^2 \boldsymbol{X}}{\partial s^2} = \frac{\partial^3 \boldsymbol{X}}{\partial s^3} = (0,0) \qquad \text{imposed at the free end,}$$

where s is the Lagrangian coordinate along the cantilever, $\boldsymbol{X}$ the cantilever's position, T the tension force serving to satisfy the inextensible condition [17], $\boldsymbol{F}_f$ the fluid loading acting on the flexible cantilever. Note the three terms on the left-hand side of Equation 1 are associated with the inertial force, tension force and bending moment, respectively.

The flow dynamics can be described by the incompressible Navier-Stokes equations

$$\frac{\partial \boldsymbol{v}}{\partial t} + \boldsymbol{v} \cdot \nabla \boldsymbol{v} = -\frac{1}{\rho_f} \nabla p + \nu \nabla^2 \boldsymbol{v} + \boldsymbol{f}_e \tag{3}$$

$$\nabla \cdot \boldsymbol{v} = 0 \tag{4}$$

where $\boldsymbol{v}$ is the flow velocity, p the pressure, ∇ the gradient operator, and $\boldsymbol{f}_e$ the external force per unit volume exerted on the flow field.

To parameterize the above fluid-structure system, the Lamb dipole's radius (R) or the cantilever length (L), the dipole's advection velocity (U), and the fluid density (ρ_f) are chosen as repeating variables. Then, Equations 1 to 4 can be non-dimensionalized as

$$m^* {L^*}^2 \frac{\partial^2 \boldsymbol{X}^*}{\partial t^{*2}} - \frac{\partial}{\partial s^*}\left(T^* \frac{\partial \boldsymbol{X}^*}{\partial s^*}\right) + \frac{\partial^2}{\partial s^{*2}}\left(EI^* \frac{\partial^2 \boldsymbol{X}^*}{\partial s^{*2}}\right) = \boldsymbol{F}_f^* \tag{5}$$

$$\frac{\partial \boldsymbol{X}^*}{\partial s^*} \cdot \frac{\partial \boldsymbol{X}^*}{\partial s^*} = 1 \tag{6}$$

$$\frac{\partial \boldsymbol{v}^*}{\partial t^*} + \boldsymbol{v}^* \cdot \nabla^* \boldsymbol{v}^* = -\nabla^* p^* + \frac{1}{Re} \nabla^{*2} \boldsymbol{v}^* + \boldsymbol{f}_e^* \tag{7}$$

$$\nabla^* \cdot \boldsymbol{v}^* = 0 \tag{8}$$

For ease of reference, the definitions of all the dimensionless parameters in Equations 5 to 8 are elaborated in Table 1 alphabetically, where the symbol "-" in the third column indicates that the corresponding parameters are updated during the simulation. The three non-dimensional parameters describing the cantilever's position relative to the Lamb dipole, i.e., the orientation angle (β), the initial horizontal and vertical distances (d_x^* and d_y^*), are also included in Table 1. Furthermore, the table also lists a dimensionless frequency f_N^* that is applied to quantify the cantilever's fundamental vibration frequency, and a dimensionless vorticity (ω^*) that is used to describe the evolution of Lamb dipole.

In this study, the cantilever's mechanical energy can be evaluated as

$$E_M = \frac{EI}{2} \int_0^L \left(\frac{\partial^2 \boldsymbol{X}}{\partial s^2}\right)^2 ds + \frac{\rho_s}{2} \int_0^L \left(\frac{\partial \boldsymbol{X}}{\partial t}\right)^2 ds \tag{9}$$

The first and second terms on the right-hand side represent the cantilever's bending energy and kinetic energy, respectively. Since the cantilever is unde-

Table 1: Definitions and selected values of dimensionless parameters in this study.

Dimensionless parameter	Definition	Values[3,4]
Initial horizontal distance	$d_x^* = d_x/R$	4
Initial vertical distance	$d_y^* = d_y/R$	0, **1/2**, 1, 3/2, 2
Stiffness	$EI^* = EI/\rho_f U^2 L^3$	1/64, 1/32, ... **1/4**, ..., 4
External force per unit volume	$\boldsymbol{f}_e^* = \boldsymbol{f}_e R/U^2$	-
Fluid loading	$\boldsymbol{F}_f^* = \boldsymbol{F}_f/\rho_f U^2$	-
Frequency[1]	$f_N^* = f_N R/U = (k_1^2/2\pi L^*)\sqrt{EI^*/m^*}$	0.03 to 0.56
Length ratio	$L^* = L/R$	1/2, 1, **2**, 4
Mass ratio	$m^* = \rho_s/\rho_f L$	1
Pressure	$p^* = p/\rho_f U^2$	-
Reynolds number	$Re = UR/\nu$	200
Lagrangian coordinate	$s^* = s/L$	-
Time	$t^* = Ut/R$	-
Tension force	$T^* = T/\rho_f U^2 L$	-
Velocity	$\boldsymbol{v}^* = \boldsymbol{v}/U$	-
Cantilever's position	$\boldsymbol{X}^* = \boldsymbol{X}/L$	-
Orientation angle	β	0, $\boldsymbol{\pi}$
Vorticity[2]	$\omega^* = \omega R/U$	-
Gradient operator	$\nabla^* = R\nabla$	-

[1] f_N is the first natural frequency of the flexible cantilever in vacuum, defined as $f_N = (k_1^2/2\pi L^2)\sqrt{EI/\rho_s}$, where $k_1 = 1.8751$ [18].

[2] ω is the dimensional vorticity.

[3] The symbol "-" indicates that the corresponding parameters are updated during the simulation.

[4] The highlighted values in the third column are used in the baseline case.

formed and stationary at the beginning, these two types of energy are both zero, thus $E_M = 0$ at $t = 0$. The work done by the fluid on the cantilever from $t = 0$ to a certain instant, i.e., τ, can be assessed as

$$W_F = \int_0^{\tau} \int_0^{L} \boldsymbol{F}_f \cdot \frac{\partial \boldsymbol{X}}{\partial t} ds dt \tag{10}$$

Based on the energy conservation law, $W_F = E_M$ all the time, i.e., the work done by the fluid on the cantilever is completely converted to the cantilever's mechanical energy, due to the omission of damping effects. The total kinetic energy carried by the entire flow field at $t = 0$ can be evaluated as [19]

$$E_T = \frac{\rho_f}{2} \int_{-\infty}^{\infty} \int_{-\infty}^{\infty} \boldsymbol{v} \cdot \boldsymbol{v} dx dy = 2\pi \rho_f U^2 R^2 \tag{11}$$

With E_T defined, E_M can be non-dimensionalized as $E_M^* = E_M / E_T$.

This study mainly aims to investigate the transfer of mechanical energy from the Lamb dipole to the deformable cantilever through their interaction. Thus, the aeroelastic efficiency is used to quantify the energy conversion efficiency, which can simply be represented by the maximum dimensionless mechanical energy of the cantilever, i.e., $\eta = \max(E_M^*)$.

2.2. Methodology

To facilitate this study, the incompressible D2Q9 MRT LBE model [20], i.e., two-dimensional incompressible multiple-relaxation-time lattice Boltzmann equation model with nine discrete velocities, is employed as an alternative numerical method for solving the two-dimensional Navier-Stokes equations. The MRT multi-block scheme proposed by Yu *et al* [21] is applied to enhance the computational efficiency while maintaining sound accuracy. The finite difference method [17, 22] is adopted for simulating the dynamics of the flexible structure governed by Equation 1 and 2. The interplay between the fluid flow and the structure dynamics is linked by the immersed boundary method (IBM) [23], which is incorporated into the lattice Boltzmann method (LBM) for coping with the moving curved boundary and accurately predicting the fluid loading exerted on the cantilever. A brief introduction to the current numerical scheme is given in Appendix, and more details of this algorithm and its validation can be found in our previous works [24, 25, 26, 27, 28]

Throughout this study, the computational domain is set as $60R \times 60R$. On its centerline is located the flexible cantilever, as shown in Figure 1. To save the computational time, the block with the finest mesh is used in the vicinity of the cantilever and the Lamb dipole, and the blocks with coarser meshes are applied in the far field.

The periodic boundary condition is implemented at the left and right boundaries of the computational domain, whereas the no-slip and no-penetration boundary conditions are imposed on the cantilever's surface as well as the top and bottom walls, as shown in Figure 1. The initial flow field is determined by applying the Lamb dipole's analytical solution [29, 30, 31, 32].

To ensure the independence of the simulation results on the mesh and time-step resolutions, three cases are selected for the convergence test, as listed in Table 2, where Δx is the finest mesh spacing and Δt the unit time step. In these three cases, the dimensionless parameters are set as $Re = 200$, $m^* = 1$, $EI^* = 1/4$, $L^* = 2$, $d_x^* = 4$, $d_y^* = 1/2$ and $\beta = \pi$. Figure 2(a) shows that the difference in the time histories of the cantilever's mechanical energy (E_M^*) up to $t^* = 20$ in these three cases are nearly indistinguishable, and the maximum E_M^* differs by less than 1%. In addition, the vorticity contours around the cantilever at $t^* = 9$ in these three cases almost overlap each other, as shown in Figure 2(b). Hence, to maintain high accuracy while saving computational effort, the mesh and time-step settings for the second case, i.e., $\Delta x = R/48$ and $U\Delta t/R = 1/4800$, are adopted throughout this study.

2.3. Case summary

To avoid discernable influence of the Lamb dipole on the cantilever at the initial stage, the initial horizontal distance (d_x^*) between the dipole and the cantilever is set as 4 throughout this study. According to Section 2.1, hence, the interactions of the flexible cantilever with the Lamb dipole and the resulting energy transfer are mainly affected by six parameters, including the Reynolds

Table 2: Selected cases for convergence test.

Parameter	Values		
	First case	Second case	Third case
Mesh spacing (Δx)	$R/48$	$R/48$	$R/96$
Advection velocity (U)	$0.02\Delta x/\Delta t$	$0.01\Delta x/\Delta t$	$0.01\Delta x/\Delta t$
Non-dimensional time step ($U\Delta t/R$)	1/2400	1/4800	1/9600

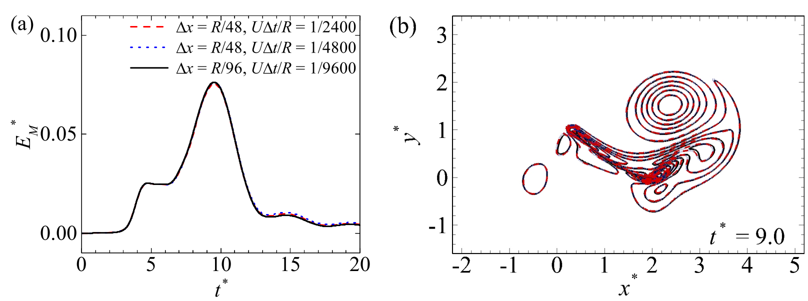

Figure 2: Results for the mesh and time-step dependence test: Time histories of the mechanical energy (E_M^*) of the cantilever from t^* = 0 to 20 (a); Vorticity (ω^*) contours [-8,8] around the cantilever at t^* = 9 (b), when Re = 200, m^* = 1, EI^* = 1/4, L^* = 2, d_x^* = 4, d_y^* = 1/2 and $\beta = \pi$.

FIG. 2. Results for the mesh and time-step dependence test: Time histories of the mechanical energy (E_M^*) of the cantilever from t^* = 0 to t^* = 20 (a); Vorticity (ω_z^*) contours [-8,8] around the cantilever at t^* = 9 (b), when Re = 200, m^* = 1, EI^* = 1/4, L^* = 2, d_x^* = 4, d_y^* = 0.5 and $\beta = \pi$. The red dashed, blue dotted and black solid lines correspond to the cases with $\Delta x = R/48$ and $U\Delta t/R$ = 1/2400, $\Delta x = R/48$ and $U\Delta t/R$ = 1/4800, and $\Delta x = R/96$ and $U\Delta t/R$ = 1/9600, respectively.

(EI^*), the length ratio (L^*), the initial horizontal and vertical distances between the Lamb dipole and the cantilever (d_x^* and d_y^*), and the orientation angle of the cantilever (β). In the present study, Re, m^* and d_x^* are set as 200, 1 and 4, respectively, for simplification. Hence, the focus of this study is placed on investigating the effects of L^*, d_y^*, EI^* and β on the energy harvesting capacity of the cantilever. Their values are determined as follows: four L^* values are selected, i.e., L^* = 0.5, 1, 2 and 4; d_y^* varies from 0 to 2 covering four different number (Re), the mass ratio (m^*), the bending stiffness (EI^*), the length ratio (L^*), the initial vertical distance between the dipole and the cantilever (d_y^*), and the orientation angle of the cantilever (β).

The Reynolds number, representing the ratio of fluid inertial force to viscous force, affects the energy dissipation in the flow system and hence the energy transferred to the cantilever. The mass ratio appearing in the first term of Equation 5 determines the cantilever's inertial force, thus affecting the force competition and the cantilever's dynamics. Although important, these two parameters are fixed at $Re = 200$ and $m^* = 1$, respectively, to focus the discussion in the present study. Hence, this study centers on exploring effects of L^*, d_y^*, EI^* and β on the energy transfer from the Lamb dipole to the cantilever. Their values are determined as follows: four L^* values are selected, i.e., $L^* = 1/2$, 1, 2 and 4; d_y^* varies from 0 to 2 covering five different values; EI^* is chosen from 1/64 to 4, being increased by a factor of 2; and β is set as 0 and π, corresponding to the cantilever's clamped end close to and away from the dipole, respectively. These selected values are listed in the third column of Table 1.

3. Results and Discussion

3.1. Overview of Results

Figure 3 gives an overview of the cantilever's aeroelastic efficiency (η or maximum E_M^*) when its length ratio is fixed at $L^* = 2$. It is found that η reaches its maximum when the initial vertical or lateral distance is in the range of $d_y^* = 1/2$ to 3/2, and the cantilever stiffness (EI^*) is around 1/4, no matter whether the cantilever is clamped upstream (i.e., $\beta = 0$, shown in Figure 3(a)) or downstream (i.e., $\beta = \pi$, shown in Figure 3(b)). This reflects that the most effective dipole-cantilever interaction occurs when the vertical distance is around the size of dipole radius and the cantilever is moderately flexible in both configurations. In this d_y^* range, η in the $\beta = \pi$ cases is generally higher than that in the $\beta = 0$ cases. This indicates that the configuration with the downstream end clamped is more favorable for the energy transfer. However, at large vertical distances,

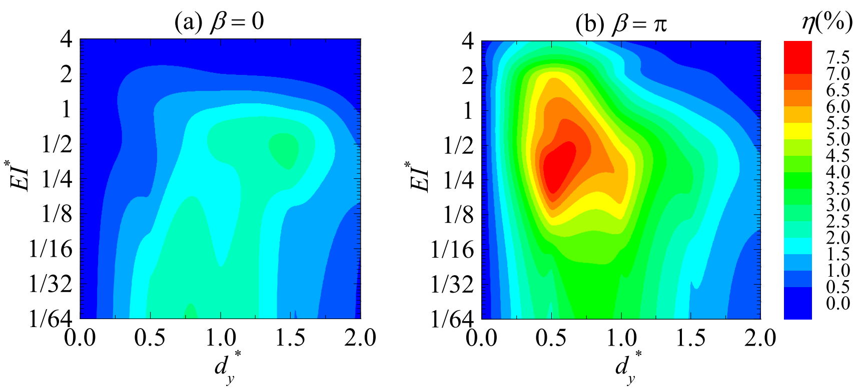

Figure 3: Contour of the aeroelastic efficiency (η) of the cantilever in the map of the initial vertical (or lateral) distance (d_y^*) versus the bending stiffness (EI^*), when the length ratio $L^* = 2$ and the orientation angle $\beta = 0$ (a) and $\beta = \pi$ (b).

e.g., $d_y^* = 2$, η is comparable in the cases with $\beta = 0$ and π, indicating that the cantilever can attain a similar amount of mechanical energy, very small though, no matter at which end it is clamped. Overall, the best efficiency among all the investigated cases $\eta = 7.6\%$ is obtained when $\beta = \pi$, $d_y^* = 1/2$ and $EI^* = 1/4$. This case is then selected as the baseline case for this study, whose parameter values have been highlighted in Table 1.

Note that based on the small-deflection and point-loading assumptions, Hu *et al.*[13] predicted that the maximum aeroelastic efficiency will be achieved roughly when the bending stiffness $EI^* = 1$ rather than $1/4$ obtained here. This discrepancy stems from the violation of the above assumptions in the current $L^* = 2$ cases, where the cantilever undergoes relatively large deformation and the fluid loading is highly temporally and spatially dependent and spreads along the entire cantilever in various patterns, as will be shown shortly. Although not presented here, it is found that as the length ratio and the vertical distance become sufficiently large, i.e., $L^* \geq 4$ and $d_y^* \geq 1$, those assumptions can be approximately satisfied, and hence the optimal bending stiffness is close to the value predicted by Hu *et al.*[13].

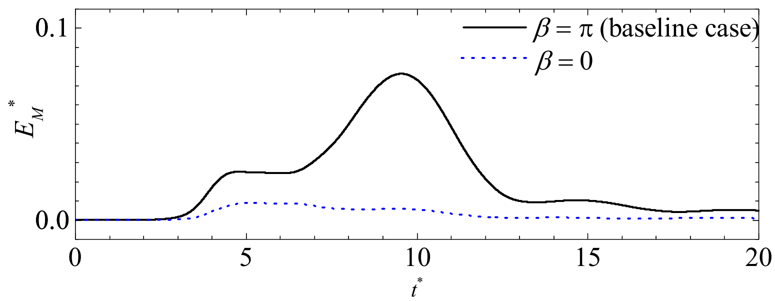

Figure 4: Time histories of the mechanical energy (E_M^*) of the cantilever for $\beta = 0$ and π, when $EI^* = 1/4$ and $d_y^* = 1/2$.

3.2. Baseline case

The time history of the cantilever's mechanical energy (E_M^*) for the baseline case is shown in Figure 4 by the solid line. It is found that E_M^* first remains unchanged, then experiences two major increases reaching its first and second peaks subsequently, and at last gradually decays towards zero. Specifically, before about $t^* = 3$, E_M^* stays close to zero due to the initial horizontal distance $d_x^* = 4$. It is also so for all the other cases investigated in this study. Therefore, for all the cases the discussion starts from $t^* = 3$ hereafter.

As time advances, the Lamb dipole gradually approaches and collides with the cantilever's free end, as evidenced by the vorticity contours and the velocity fields around the cantilever at $t^* = 3$ and 4 shown in Figures 5(a1) and 5(a2), respectively. During this period, the forward and downward flow induced by the dipole's lower core impinges on the cantilever's upper surface, resulting in large downward-oriented fluid loading acting on the cantilever, and hence promoting the cantilever's fast downward deflection, as shown in Figures 5(b1), 5(c1), 5(b2) and 5(c2). Since the fluid loading and the cantilever velocity are both oriented downwards during this period, the fluid does positive work on the cantilever, i.e., the energy is transferred from the fluid to the cantilever. Under this circumstance, E_M^* rapidly increases and approaches its first peak roughly at $t^* = 4.5$, as shown in Figure 4.

At around $t^* = 5$, the cantilever achieves its maximum downward deflection

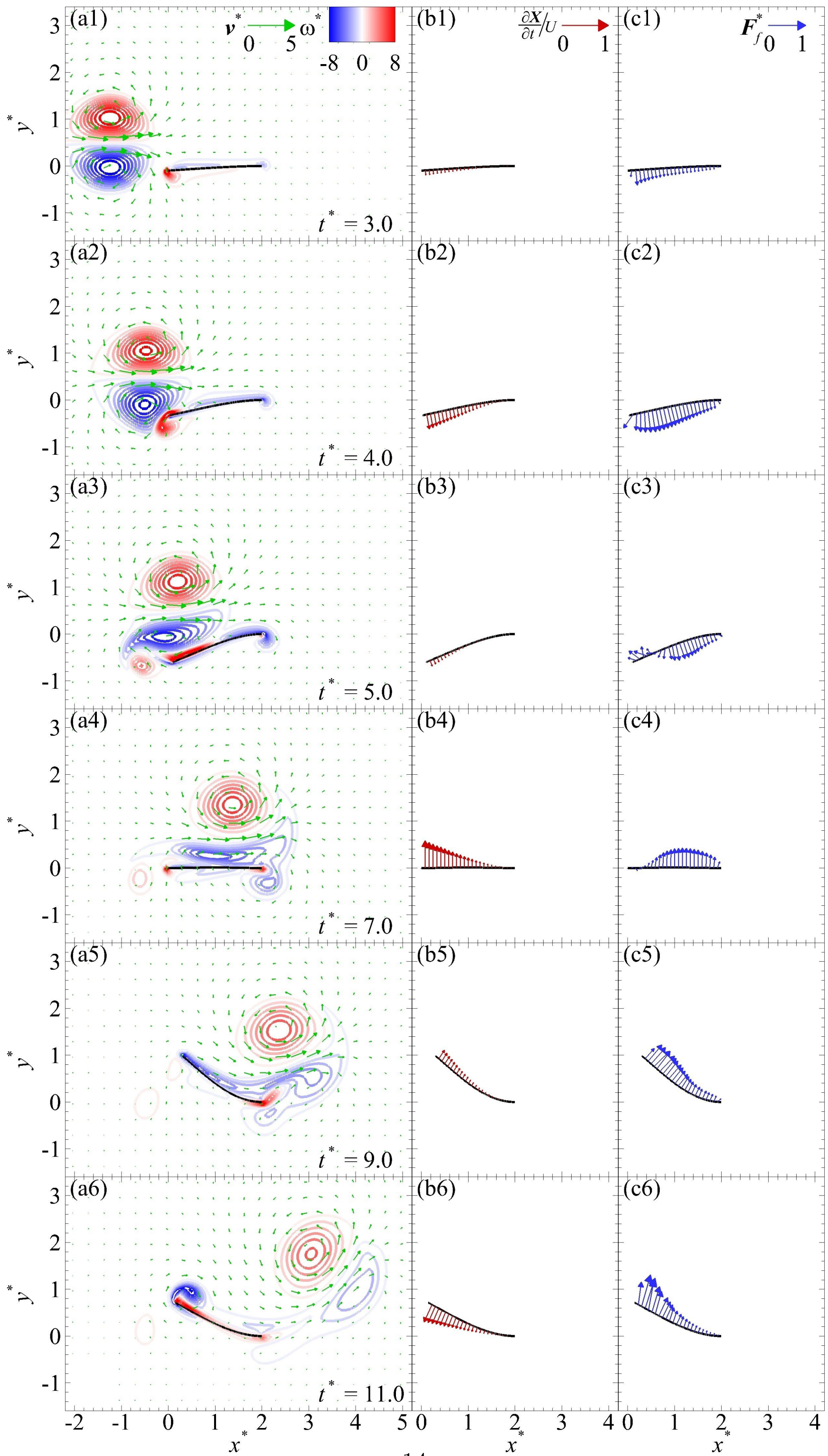

Figure 5: Vorticity (ω^*) contours and velocity ($\boldsymbol{v}^*$) fields around the cantilever (the first column) as well as the velocity ($\frac{\partial \boldsymbol{X}}{\partial t}/U$, the second column) and fluid loading ($\boldsymbol{F}_f^*$, the third column) distributions along the cantilever at t^* = 3 [(a1) to (c1)]; t^* = 4 [(a2) to (c2)]; t^* = 5 [(a3) to (c3)]; t^* = 7 [(a4) to (c4)]; t^* = 9 [(a5) to (c5)]; t^* = 11 [(a6) to (c6)], for the baseline case.

and is about to recover its original shape, as indicated by the third row of Figure 5. The dipole's lower core, corresponding to a low-pressure region, reaches the cantilever's free end and induces upward-oriented fluid loading there. Meanwhile, the induced forward and downward flow ahead of the dipole core continues impacting on the cantilever's downstream part. Since the direction of the fluid loading near the free end is opposite to that in the downstream part, the work done by the fluid on these two parts can offset each other near this instant, leading to negligible total work on the cantilever. This kind of fluid loading distribution persists until around $t^* = 6$. Accordingly, almost no net energy exchange can be observed between the fluid and the cantilever approximately from $t^* = 5$ to 6, resulting in the E_M^* plateau shown in Figure 4.

As time progresses to $t^* = 7$, the cantilever completely returns to its original shape, and is about to deflect upwards with a relatively large speed appearing at its free end, as indicated in Figure 5(b4). At this instant, the dipole's lower core is squeezed and elongated so that it almost covers the cantilever's entire upper surface. In the meantime, its induced flow first circumnavigates the clamped end and then impinges on the cantilever's lower surface. These two factors, therefore, collaboratively result in the upward-oriented fluid loading nearly along the entire cantilever. Under this condition, fluid starts to do positive work on the cantilever again, leading to the second round of increase in E_M^*, as shown in Figure 4. Afterward, the cantilever continues deflecting upwards, and the fluid loading consistently keeps upward-oriented, as evidenced by the fifth row of Figure 5. As such, the fluid continues transferring energy to the cantilever. Immediately after $t^* = 9$, E_M^* approaches its second and also higher peak, i.e., $\max(E_M^*) = \eta = 7.6\%$, and the cantilever also reaches its maximum upward deflection.

Approximately at $t^* = 10$, the cantilever starts to recover its original shape, as shown in Figure 5(b6). Meanwhile, the Lamb dipole progressively moves away from it, as shown in Figure 5(a6). Since then, the dipole makes negligible impact on the cantilever's dynamics, and the fluid loading always points in the opposite direction of the cantilever's motion, as demonstrated in Figures 5(b6) and 5(c6). As such, the mechanical energy stored in the cantilever is transferred back to the fluid, leading to the consistent decrease in E_M^* until the cantilever stops moving. During this period, the fluid surrounding the cantilever essentially works as a damper.

From the above discussions, it is seen that the pace of the cantilever's deflection perfectly matches that of the dipole's advection. That is, when the dipole approaches the cantilever's free end, it induces downward-oriented fluid loading along almost the entire cantilever that causes the cantilever to deflect downwards. As the dipole is right above the cantilever's free end and exerts suction, the cantilever just returns to its original shape from downwards, hence its free end can take advantage of this suction to further promote the energy transfer. When the dipole further moves towards the cantilever's clamped end and exerts upward-oriented fluid loading on the cantilever, the entire cantilever deflects upwards to extract the energy. Through these interactions, the cantilever consistently receives energy from the passing dipole and attains the most energy from it.

It is also interesting to see that the Lamb dipole's trajectory deviates from its original advection direction as it leaves the cantilever, as shown in Figure 5(a6). This is because the strength of the dipole's lower core is significantly reduced through its interaction with the cantilever, while the upper core is not affected too much. As such, the dipole becomes unbalanced and its trajectory curls counterclockwise above the cantilever.

3.3. Effects of orientation angle

Figure 3 has shown the overwhelming advantages of the cantilever with the orientation angle $\beta = \pi$ over that with $\beta = 0$ in the energy transfer when the initial vertical distance d_y^* varies between 1/2 and 3/2. To explore the reason, one representative case, i.e., the case very similar to the baseline case except its orientation angle $\beta = 0$, is selected for a comparison.

Figure 4 compares the time histories of the cantilever's mechanical energy E_M^* in the selected case and in the baseline case. It is seen that E_M^* in the $\beta = 0$

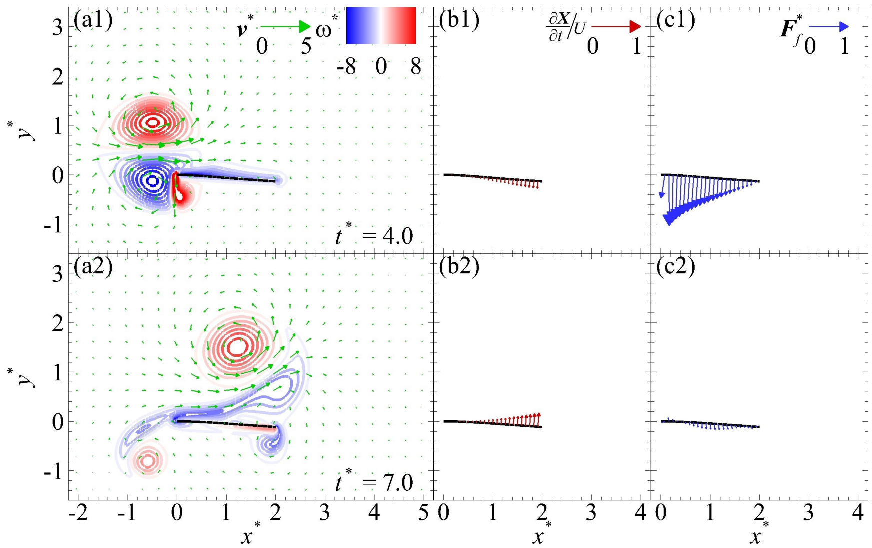

Figure 6: Vorticity (ω^*) contours and velocity ($\boldsymbol{v}^*$) fields around the cantilever (the first column) as well as the velocity ($\frac{\partial \boldsymbol{X}}{\partial t}/U$, the second column) and fluid loading ($\boldsymbol{F}_f^*$, the third column) distributions along the cantilever at $t^* = 4$ [(a1) to (c1)] and $t^* = 7$ [(a2) to (c2)] for the case with $d_y^* = 1/2$, $EI^* = 1/4$ and $\beta = 0$.

case is much smaller during the dipole-cantilever interaction period. Obviously this significant change is caused by the swap of the cantilever's two-end conditions. As revealed in Figure 6(a1), at around $t^* = 4$ the Lamb dipole makes a very hard impact on the cantilever's upstream, clamped end, losing the coherence and much strength in its lower core. As a result, the dipole becomes evidently unbalanced and deviates from the cantilever much earlier, i.e., before $t^* = 7$, as evidenced by Figure 6(a2). In addition, unlike in the baseline case, only one major E_M^* increase is observed from $t^* = 3$ to 5, which is also much milder, as shown in Figure 4. This increase is also caused by the induced forward and downward flow ahead of the dipole's lower core. However, since in this case the cantilever's upstream end is clamped and its downstream end is free, only the weak downward fluid loading near the free end makes contributions to the downward deflection, as revealed in the first row of Figure 6. After this E_M^* increase, the dipole leaves the cantilever very soon, and hence the second E_M^*

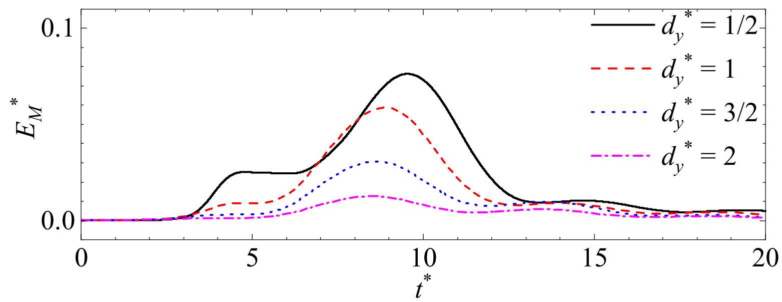

Figure 7: Time histories of the mechanical energy (E_M^*) of the cantilever for the cases with $d_y^* = 0$, 1/2, 1, 3/2 and 2 when $EI^* = 1/4$ and $\beta = \pi$.

increase is not observed. For these reasons, the interaction between the dipole and the cantilever in the $\beta = 0$ case is much weaker in strength and shorter in time, which explains the much less energy transfer.

3.4. Effects of vertical distance

To explore the effects of the vertical distance (d_y^*), three cases are selected, in which the vertical distance is set as $d_y^* = 1$, 3/2 and 2, respectively, while the other parameters remain the same as those in the baseline case. Figure 7 reveals that the time histories of the mechanical energy (E_M^*) in all the three cases are similar to that in the baseline case. This means that the influences on the cantilever exerted by the Lamb dipole at different vertical distances are similar, and so is the cantilever's dynamics. Specifically, akin to in the baseline case, in these cases the Lamb dipole first pushes the cantilever downwards, and then pulls the cantilever as it reverts to its original shape and starts the upward deflection. This can be evidenced by comparing among these cases the vorticity contours as well as the velocity and fluid loading distributions along the cantilever at around $t^* = 4$ and 6.5, as shown in Figures 5, 8 and 9.

Differences are also discernable among these cases. With the increase of d_y^*, the dipole-cantilever interaction becomes weaker, so that the energy transferred to the cantilever generally decreases, as revealed in Figure 7. In addition, the advection of the Lamb dipole is less hindered by the cantilever, resulting

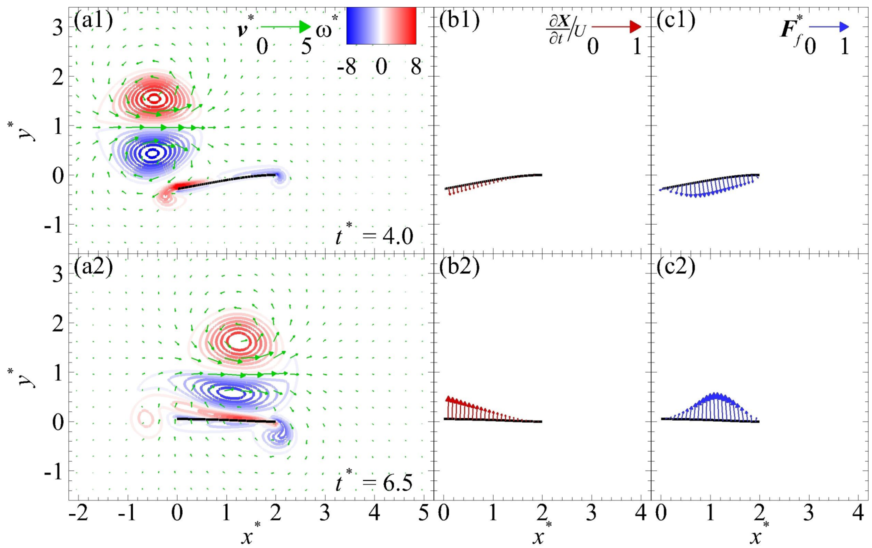

Figure 8: Vorticity (ω^*) contours and velocity ($\boldsymbol{v}^*$) fields around the cantilever (the first column) as well as the velocity ($\frac{\partial \boldsymbol{X}}{\partial t}/U$, the second column) and fluid loading ($\boldsymbol{F}_f^*$, the third column) distributions along the cantilever at $t^* = 4$ [(a1) to (c1)] and $t^* = 6.5$ [(a2) to (c2)] for the case with $d_y^* = 1$, $EI^* = 1/4$ and $\beta = \pi$.

in earlier and faster interaction. As such, the cantilever's mechanical energy approaches its maximum earlier. Figure 7 also reveals that, when the vertical distance is sufficiently large, e.g., $d_y^* = 2$, the pushing effect becomes negligible as evidenced by the nearly zero mechanical energy at around $t^* < 5$. Under this circumstance, the energy transfer mainly occurs during the cantilever's upward deflection, when the Lamb dipole is right above the cantilever and pulls it upwards, as snapshot in the last row of Figure 9. On the other hand, when d_y^* is very small approaching zero, the Lamb dipole tends to be bisected by the cantilever, and the fluid loading on the cantilever's upper and lower surfaces is likely to cancel out each other. As such, the cantilever is almost stationary and attains nearly zero mechanical energy, as having been confirmed in Figure 3.

Among the cases compared in this subsection, the baseline case with $d_y^* = 1/2$ achieves the maximum aeroelastic efficiency. This is different from what has been reported by Pirnia *et al.*[16]. In their study, a flexible plate is initially

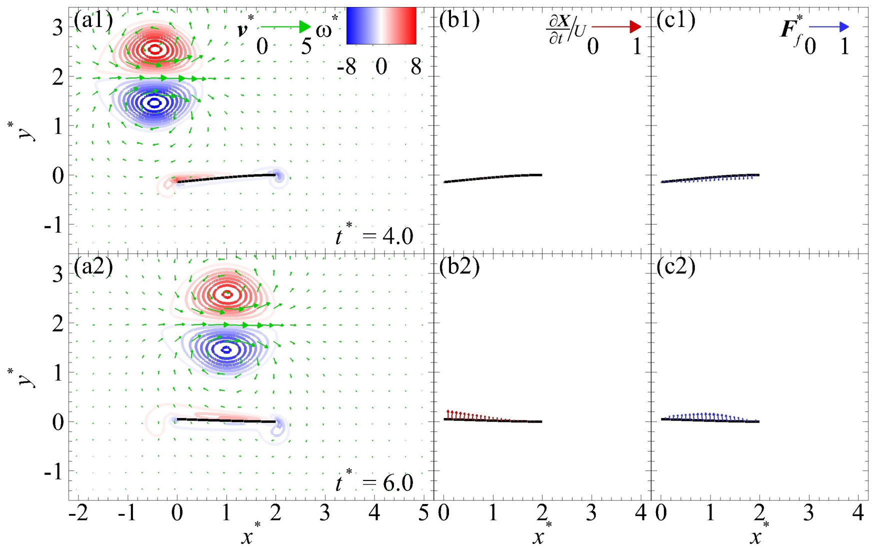

Figure 9: Vorticity (ω^*) contours and velocity ($\boldsymbol{v}^*$) fields around the cantilever (the first column) as well as the velocity ($\frac{\partial \boldsymbol{X}}{\partial t}/U$, the second column) and fluid loading ($\boldsymbol{F}_f^*$, the third column) distributions along the cantilever at $t^* = 4$ [(a1) to (c1)] and $t^* = 6$ [(a2) to (c2)] for the case with $d_y^* = 2$, $EI^* = 1/4$ and $\beta = \pi$.

placed against the advection direction of a vortex ring, and its bending stiffness, mass ratio and length ratio are approximately $EI^* = 1.09$, $m^* = 2.44$ and $L^* = 5.56$, respectively. They found that the maximum aeroelastic efficiency can be achieved when the distance ratio (defined as the ratio of the distance of the vortex-ring centerline from the plate to the radius of the vortex ring, and equivalent to d_y^*) is around 1.37, approximately corresponding to the condition where the edge of the vortex ring is tangential to the plate. When the distance ratio is smaller than this value, the vortex ring is less favorable for the energy transfer due to the decrease in the pressure loading. Although not shown here for the sake of brevity, this optimum distance ratio is confirmed to some extent by one set of our cases with the closest parameter values, i.e., $L^* = 4$, $EI^* = 1$ and $\beta = \pi$, where the optimum vertical distance is $d_y^* = 1$, corresponding to the condition that the edge of the Lamb dipole is initially tangential to the cantilever. Furthermore, it is found that this optimum d_y^* is not a constant.

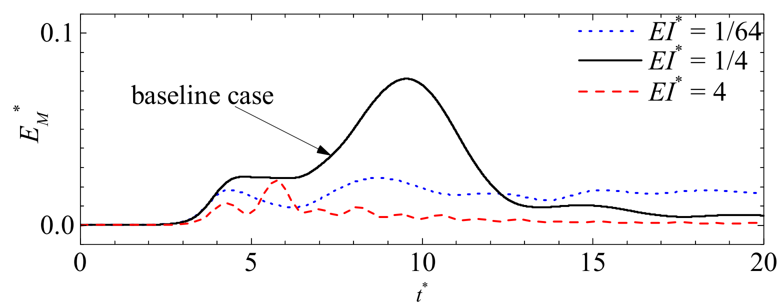

Figure 10: Time histories of the mechanical energy (E_M^*) of the cantilever for the cases with EI^* = 1/64, 1/4 and 4 when d_y^* = 1/2 and $\beta = \pi$.

Instead, it can be affected by other parameters, such as the length ratio and the bending stiffness. In some cases such as the cases discussed in this subsection where $L^* = 2$, $EI^* = 1/4$ and $\beta = \pi$, it can be smaller than 1 due to the cantilever's larger downward deflection and hence the milder impact of the Lamb dipole on the cantilever's free end. Nevertheless, despite the discrepancy in the actual values, both Pirnia *et al.*[16] and our study confirm that the optimal d_y^* should not be either very small or very large.

3.5. Effects of stiffness

To further study the influence of the cantilever's stiffness, two cases are chosen for comparison: one with $EI^* = 1/64$ is 16 times more flexible than the baseline case (denoted as the most flexible case), and the other with $EI^* = 4$ is 16 times stiffer (denoted as the stiffest case).

In the most flexible case, at the beginning of the dipole-cantilever interaction, i.e., at $t^* \leq 4$, the variation of the cantilever's mechanical energy E_M^* appears almost the same as in the baseline case, as shown in Figure 10. During this period the inertial force and fluid loading exerted on the cantilever are very similar to those in the baseline case because of the same initial conditions. Although the restoring bending moments in these two cases differ by about one order of magnitude, they are both small at this stage and hardly affect the cantilever's dynamics. As a result, the dynamics of the cantilever and the dipole

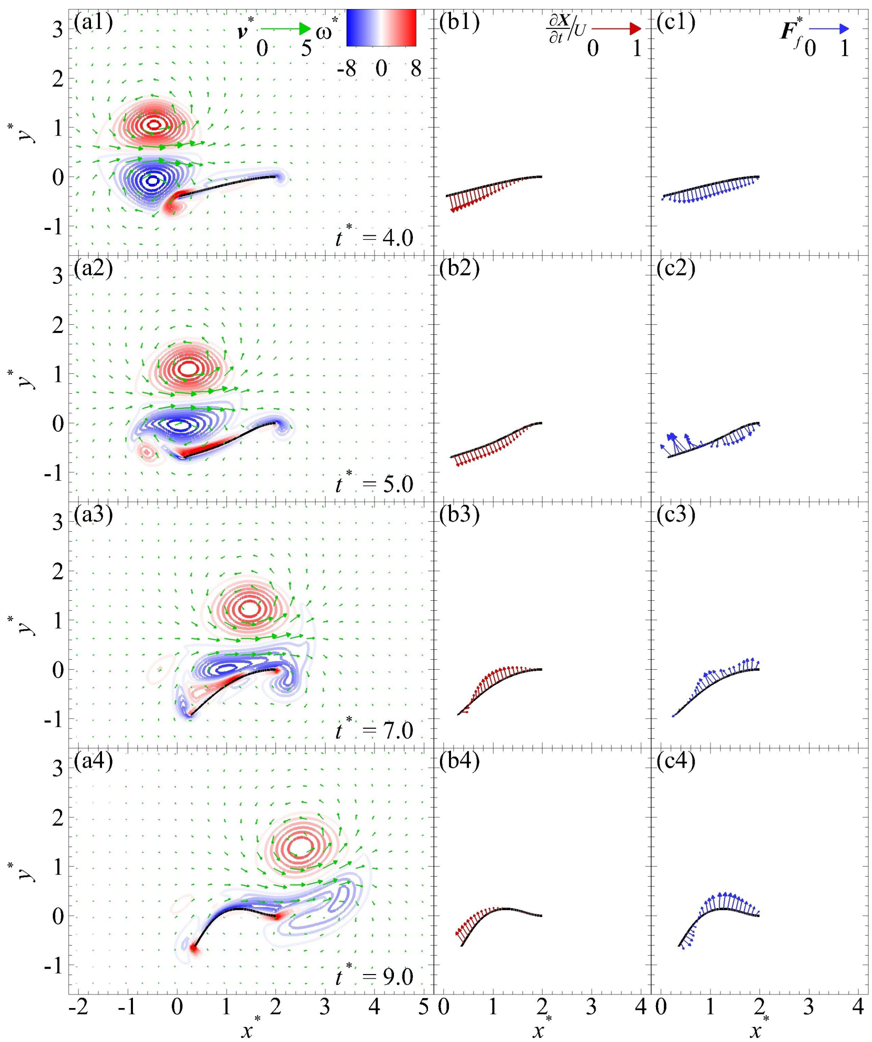

Figure 11: Vorticity (ω^*) contours and velocity ($\boldsymbol{v}^*$) fields around the cantilever (the first column) as well as the velocity ($\frac{\partial \boldsymbol{X}}{\partial t}/U$, the second column) and fluid loading ($\boldsymbol{F}_f^*$, the third column) distributions along the cantilever at t^* = 4 [(a1) to (c1)]; t^* = 5 [(a2) to (c2)]; t^* = 7 [(a3) to (c3)]; t^* = 9 [(a4) to (c4)], when d_y^* = 1/2, EI^* = 1/64 and $\beta = \pi$.

becomes very similar in these two cases, as evidenced by comparing the second row of Figure 5 with the first row of Figure 11. A similar amount of energy is then transferred from the fluid to the cantilever during this period.

After about $t^* = 4$, E^*_M in the most flexible case approaches its first peak, which is followed by an apparent decrease rather than remaining almost unchanged in the baseline case, as shown in Figure 10. When the cantilever becomes more flexible, its much less bending moment is not able to stop the cantilever from further deflecting downward at this instant, as evidenced in Figure 11(b2). Meanwhile, the upward-oriented fluid loading near the cantilever's free end in this case is larger than in the baseline case, whereas the downward-oriented fluid loading at the rest part is smaller, as shown in Figures 5(c3) and 11(c2). As such, the fluid does less positive or even negative net work on the cantilever, responsible for the smaller peak and the following decrease in E^*_M.

At around $t^* = 6$, E^*_M in the most flexible case reaches its local minimum and starts to increase again towards its second peak. The cantilever's free end approaches its lowest position at about $t^* = 7$, as shown in Figure 11(b3), much delayed if compared with that in the baseline case. As such, the lower core of the Lamb dipole is farther away from the free end, and hence exerts less suction and yields smaller upward-oriented fluid loading on the cantilever, as shown in Figures 5 and 11. In addition, the cantilever notably displays deflection of higher-order modes, e.g., at $t^* = 9$. Hence the fluid loading scatters in various directions, as shown in Figure 11(c4). The energy transfer between the fluid and the cantilever is therefore complicated and not just in one way. Furthermore, the Lamb dipole leaves the cantilever at about $t^* = 9$, stopping exchanging energy with the cantilever. All these factors explain the smaller E^*_M increasing rate towards the second peak and the much smaller peak value shown in Figure 10.

In the stiffest case, the cantilever is more refrained by the bending moment, thus undergoes much less deformation than in the baseline case. Consequently, the cantilever interacts more intensely with the Lamb dipole, and experiences much larger fluid loading. This can be evidenced by comparing the fluid loading distribution in these two cases at $t^* = 4$, as shown in Figures 5(c2) and 12(c1).

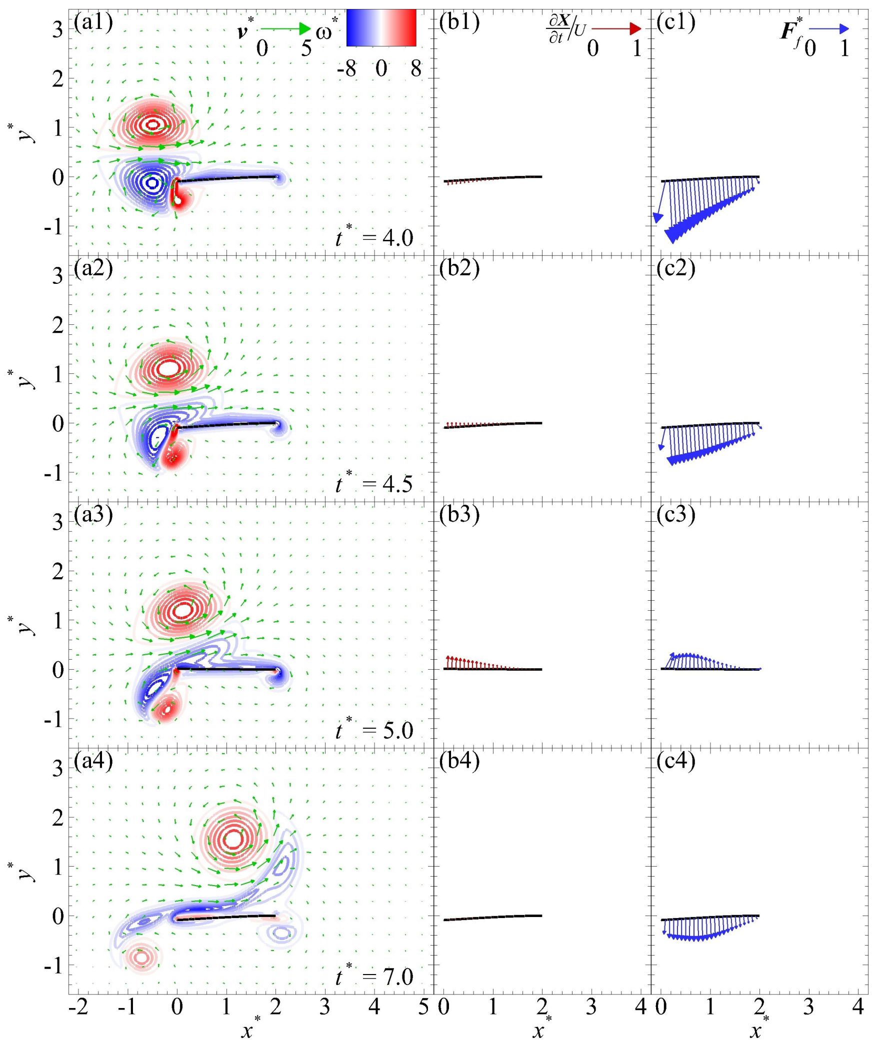

Figure 12: Vorticity (ω^*) contours and velocity ($\boldsymbol{v}^*$) fields around the cantilever (the first column) as well as the velocity ($\frac{\partial \boldsymbol{X}}{\partial t}/U$, the second column) and fluid loading ($\boldsymbol{F}_f^*$, the third column) distributions along the cantilever at t^* = 4 [(a1) to (c1)]; t^* = 4.5 [(a2) to (c2)]; t^* = 5 [(a3) to (c3)]; t^* = 7 [(a4) to (c4)], when d_y^* = 1/2, EI^* = 4 and $\beta = \pi$.

On the other hand, at this instant the cantilever's velocity in the stiffest case is remarkably smaller, as shown in Figures 5(b2) and 12(b1), due to the significant increase in stiffness and hence in the restoring bending moment. As a result of these two counteracting factors, it is seen that the E^*_M increasing rate is slightly smaller than in the baseline case, as shown in Figure 10.

Due to the significantly larger restoring bending moment, the stiffest cantilever returns to its original position very soon, during which its velocity changes the direction from downwards to upwards, as revealed in Figures 12(b1) and 12(b2). Meanwhile, the fluid loading keeps pointing downwards during this period, as shown in 12(c1) and 12(c2). Hence the energy transfer reverses its direction and E^*_M stops increasing. This explains the much earlier and smaller first peak right after $t^* = 4$ in the stiffest case, as shown in Figure 10.

Similar to in the baseline case, the second notable increase in E^*_M and the associated peak appearing from about $t^* = 5$ to 6 are also caused by the suction of the dipole's lower core. At $t^* = 5$, the fluid loading over the cantilever just turns upwards due to the suction, and the cantilever also happens to deflect upwards, as shown in the third row of Figures 12. As such, E^*_M increases rapidly. However, since under the strong restoring bending moment the cantilever promptly reverses its deflection motion right before $t^* = 6$, this fluid-to-cantilever energy transfer lasts for a much shorter time than in the baseline case, hence resulting in a much smaller second E^*_M peak.

At $t^* = 7$, the Lamb dipole starts to leave the cantilever, as shown in Figure 12(a4), after which it stops exchanging energy with the cantilever, leading to a consistent decrease in E^*_M. The leaving of the dipole occurs much earlier than in the baseline case, because the dipole becomes more unbalanced after its more intense collision with the stiffest cantilever, as evidenced by comparing Figure 5(a2) with Figure 12(a1).

It is noteworthy that, according to Equation 5 and the definition of f^*_N, the cantilever's dimensionless first natural frequency as listed in Table 1, studying the effect of EI^* is equivalent to studying the effect of f^*_N for given mass ratio m^* and length ratio L^*. As such, the discussion on the effect of EI^* in this

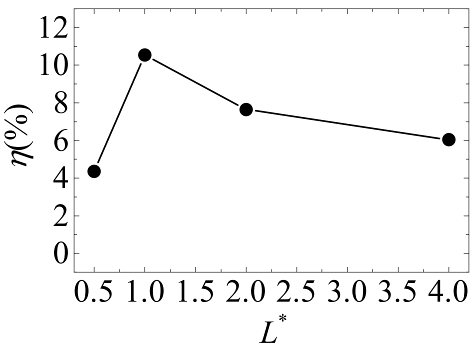

Figure 13: Variations of the aeroelastic efficiency (η) of the cantilever against the length ratio (L^*), when $d_y^* = 1/2$, $EI^* = 1/4$ and $\beta = \pi$.

subsection also suggests that an optimum f_N^* exists, with which the cantilever's deflection pace matches the dipole's advection pace, leading to significantly higher aeroelastic efficiencies.

3.6. Effects of cantilever length

In all the cases discussed above the cantilever's length ratio is fixed at $L^* = 2$. Apparently L^* also affects the dipole-cantilever interaction and the resulting energy transfer. Hence, its effects are explored in this section. Figure 13 shows the variation of the aeroelastic efficiency η against L^* in the range of 1/2 to 4, while the other parameters remaining the same as in the baseline case. It is found that η achieves its maximum 10.6% at $L^* = 1$, indicating that the cantilever with a length close to the dipole radius is able to receive the largest amount of energy from the dipole.

Time histories of the cantilevers' mechanical energy (E_M^*) in the four selected cases are compared in Figure 14. In all the cases E_M^* shows a similar variation trend. That is, E_M^* significantly increases twice, resulting in two major peaks, where the second peaks are much larger than the first peaks. It is observed that the longer the cantilever is, the later its E_M^* peaks appear. This is not unexpected since the cantilever's fundamental resonant frequency is approximately inversely proportional to its length L^*, as indicated in the formula

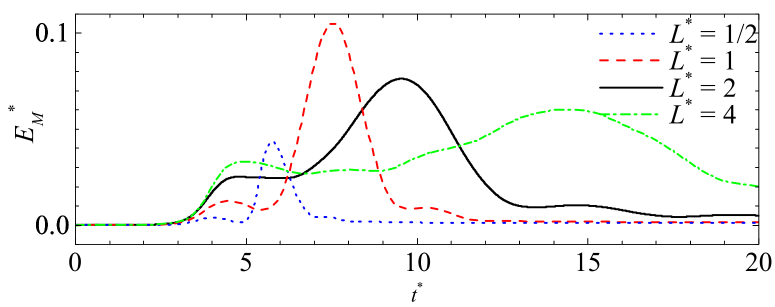

Figure 14: Time histories of the mechanical energy (E_M^*) of the cantilever for the cases with $L^* = 1/2$, 1, 2 and 4, when $d_y^* = 1/2$, $EI^* = 1/4$ and $\beta = \pi$.

listed in Table 1.

From Figure 14, it is also observed that the first E_M^* peak increases with the cantilever length. Since the first peak corresponds to the dipole-to-cantilever energy transfer during the cantilever's first downward deflection, the longer the cantilever is, the more impact it can receive from the dipole, and hence the more energy can be transferred. However, it is expected that this increasing trend will gradually become marginal once the cantilever length is far larger than the dipole size, which can be deduced from the relative increasing rate of the first peaks in the four selected cases. As for the second E_M^* peak, it corresponds to the energy transfer during the cantilever's first upward deflection when the dipole moves away from the free end. The shorter the cantilever is, the faster it responds, so that its free end can follow the dipole's pace more easily and hence experiences much stronger dipole-induced suction. As such, in general a shorter cantilever can attain more energy at this stage. However, if the cantilever is too short compared to the size of the dipole, such as in the case with $L^* = 1/2$, the transferred energy it can store also reduces. This explains why the maximum second E_M^* peak appears in the $L^* = 1$ case, where the cantilever is short but comparable in size with the dipole.

4. Conclusion

In this study we investigated the energy transfer from an advecting Lamb dipole to an elastic cantilever. The cantilever has a fixed mass ratio 1 and is placed either along or against the dipole's advection direction. At a fixed Reynolds number of 200, we studied the detailed interaction between the cantilever and the dipole, and explored the effects of their initial vertical distance (d_y^*) and the cantilever's orientation angle (β), bending stiffness (EI^*) and length (L^*) on the transferred energy (E_M^*) and the aeroelastic efficiency (η). The major findings are as follows:

1. When the initial vertical distance is very small ($d_y^* \approxeq 0$) or sufficiently large ($d_y^* \geq 2$), the transferred energy is marginal, no matter at which end the cantilever is clamped. At moderate d_y^*, i.e., approximately in the range of 1/2 to 3/2, the strong dipole-cantilever interaction is favorable for energy transfer. Also, placing the cantilever against the dipole's advection direction (i.e., with $\beta = \pi$) is more favorable for energy transfer compared to placing it in the opposite way (i.e., with $\beta = 0$).

2. When placed against the dipole's advection direction, the cantilever generally experiences two notable increases in its mechanical energy E_M^*. The first one occurs during the first downward deflection that is caused by the direct impact associated with the dipole's approach, whereas the second one occurs during the first upward deflection when the dipole just passes by and exerts suction on the free end. Each E_M^* increase results in a peak, and the second peak is much higher than the first peak, indicating the dominant role of the dipole suction in the energy transfer.

3. If the cantilever's length is fixed at $L^* = 2$, the baseline case performs the best. In this case, the cantilever is placed against the dipole's advection direction, and its moderate initial vertical distance $d_y^* = 1/2$ and bending stiffness $EI^* = 1/4$ result in a favorable FSI, such that the cantilever's deflection pace matches the dipole's advection pace. Hence, the flow energy

can be consistently transferred to the cantilever, leading to the maximum efficiency $\eta = 7.6\%$.

4. Changing the cantilever's bending stiffness changes its response to the flow. If becoming more flexible, the cantilever takes more time to reverse its deflection direction to catch up with the dipole's suction. In addition, it experiences deflection of high-order modes, resulting in scattered fluid loading and much less energy transfer. If becoming stiffer, the cantilever reverses its deflection direction sooner, even before the dipole starts exerting the suction. In both cases, the cantilever's deflection does not match with the dipole's advection pace and hence less energy is transferred to it if compared with the baseline case.

5. The cantilever length also affects the energy transfer. The longer the cantilever is, the later its E_M^* peaks appear. The first E_M^* peak increases with the cantilever length. In general, the second E_M^* peak increases with the decrease of the cantilever length. However, if the cantilever is too short compared to the size of dipole, such as $L^* = 1/2$, the maximum transferred energy it can store reduces. Overall, it is found that the maximum aeroelastic efficiency of 10.6% occurs when the cantilever length is close to the dipole's radius, i.e., $L^* = 1$.

Although not shown here for brevity, it is found that as the Reynolds number increases, more mechanical energy can be attained by the cantilever. This results from the fact that the fluid kinetic energy is less dissipated at higher Reynolds numbers. Nevertheless, the dipole-cantilever interaction and the resulting cantilever dynamics are still very similar over a wide range of Reynolds numbers. This suggests that the energy transfer process and the effects of key parameters as revealed at $Re = 200$ in this study do not change too much over a wide range of Reynolds numbers.

This study furthers our understanding in the energy transfer from an advecting Lamb dipole to a flexible cantilever, through investigating their detailed

FSI. Although insightful, the effects of several other key parameters, such as the mass ratio and general orientation angle, are not explored. They will be systematically investigated in our near-future work.

Acknowledgments

We gratefully acknowledge the financial support for this study from the Research Grants Council of Hong Kong under General Research Fund (Project No. PolyU 152493/16E) and the Departmental General Research Fund (Project No. G-UA5A & G-YBLP) from the Department of Mechanical Engineering of The Hong Kong Polytechnic University.

Appendix

Immersed boundary lattice Boltzmann method

In this study, the lattice Boltzmann method (LBM) is adopted as an alternative numerical method for solving the Navier-Stokes equations represented by Equations 3 and 4. Specifically, the incompressible D2Q9 MRT LBE model, i.e., two-dimensional incompressible multiple-relaxation-time lattice Boltzmann equation model with nine discrete velocities, is used for the simulation, which can be expressed as [20, 23]

$$\begin{aligned} f_\alpha\left(\boldsymbol{x}+\boldsymbol{c}_\alpha \Delta t, t+\Delta t\right)-f_\alpha(\boldsymbol{x}, t)= & -\boldsymbol{M}^{-1} \boldsymbol{S} \boldsymbol{M}\left(f_\alpha(\boldsymbol{x}, t)-f_\alpha^{e q}(\boldsymbol{x}, t)\right) \\ & -\boldsymbol{M}^{-1}(\boldsymbol{I}-\boldsymbol{S} / 2) \boldsymbol{M} g_\alpha(\boldsymbol{x}, t) \Delta t \end{aligned} \tag{12}$$

where f_α is the distribution function with α indicating its propagation direction, $\boldsymbol{x}$ the Eulerian coordinate, $\boldsymbol{c}_\alpha$ the lattice velocity, t the time, Δt the unit time step, $\boldsymbol{M}$ the transformation matrix, $\boldsymbol{S}$ the non-negative diagonal relaxation matrix containing different relaxation rates, $\boldsymbol{I}$ the identity matrix, and f_α^{eq} the local equilibrium distribution function which can be written as

$$f_\alpha^{eq}=w_\alpha\left[\rho_f+\rho_{f0}\left(\frac{\boldsymbol{c}_\alpha \cdot \boldsymbol{v}}{c_s^2}+\frac{\left(\boldsymbol{c}_\alpha \cdot \boldsymbol{v}\right)^2}{2 c_s^4}-\frac{\boldsymbol{v}^2}{2 c_s^2}\right)\right] \tag{13}$$

w_α is the weighting factor, ρ_f the fluid density, ρ_{f0} the mean fluid density, $\boldsymbol{v}$ the fluid velocity, and c_s the sound speed of the fluid. The fluid velocity $\boldsymbol{v}$ and the fluid density ρ_f can be evaluated by the distribution function f_α and the lattice velocity $\boldsymbol{c}_\alpha$ as follows,

$$\rho_{f0}\boldsymbol{v} = \sum_\alpha \boldsymbol{c}_\alpha f_\alpha \tag{14}$$

$$\rho_f = \sum_\alpha f_\alpha \tag{15}$$

In Equation 12, g_α is the discrete force distribution function which can be evaluated as [23]

$$g_\alpha = w_\alpha \left(\frac{\boldsymbol{c}_\alpha - \boldsymbol{v}}{c_s^2} + \frac{\boldsymbol{c}_\alpha \cdot \boldsymbol{v}}{c_s^4} \boldsymbol{c}_\alpha \right) \cdot \boldsymbol{f}_e \tag{16}$$

where $\boldsymbol{f}_e$ is the external force per unit volume in Equation 3.

In addition, Equations 1 and 2 governing the dynamics of the flexible structure are discretized using the finite difference method for the simulation [22, 17]. To resolve the interplay between the fluid flow and the structure dynamics, i.e., to properly impose the no-slip and no-penetration boundary conditions on the cantilever's surface, the immersed boundary method (IBM) is adopted and the discretized IBM formulations suggested by Kang [23] are utilized in this study, which can be expressed

$$\boldsymbol{v}_b = \sum \boldsymbol{v}\delta\left(\boldsymbol{x} - \boldsymbol{X}\right)\Delta x^2 \tag{17}$$

$$\boldsymbol{F}_f = -2\rho_f \frac{\frac{\partial \boldsymbol{X}}{\partial t} - \boldsymbol{v}_b}{\Delta t} \tag{18}$$

$$\boldsymbol{f}_e = -\sum \boldsymbol{F}_f \delta\left(\boldsymbol{x} - \boldsymbol{X}\right)\Delta s \tag{19}$$

where $\boldsymbol{v}_b$ is the unforced velocity of the flexible structure interpolated from the velocity $\boldsymbol{v}$ of the ambient flow through the regularized discrete delta function δ, $\boldsymbol{F}_f$ is the fluid loading acting on the structure in Equation 1 that is related to the difference between the actual velocity $\partial\boldsymbol{X}/\partial t$ of the structure and its unforced velocity $\boldsymbol{v}_b$, $\boldsymbol{f}_e$ is the external force per unit volume in Equation 3 evaluated by the fluid loading $\boldsymbol{F}_f$ through the delta function δ, $\boldsymbol{X}$ is the structure position, and Δx and Δs are the mesh spacings for the computational fluid and solid domains, respectively.

With the above IBM implemented into the incompressible D2Q9 MRT LBE model, the fluid-structure interaction (FSI) problem involved in this study can be accurately solved. More details of the current numerical algorithm and its validation can be found in our previous works [24, 25, 26, 27, 28]

References

[1] E. Sazonov, H. Li, D. Curry, P. Pillay, Self-powered sensors for monitoring of highway bridges, IEEE Sens. J. 9 (11) (2009) 1422–1429.

[2] Y. Cha, W. Chae, H. Kim, H. Walcott, S. Peterson, M. Porfiri, Energy harvesting from a piezoelectric biomimetic fish tail, Renewable Energy 86 (2016) 449–458.

[3] S. Priya, D. Inman, Energy harvesting technologies, Vol. 21, Springer, 2009.

[4] N. Elvin, A. Erturk, Advances in energy harvesting methods, Springer Science & Business Media, 2013.

[5] H. D. Akaydin, N. Elvin, Y. Andreopoulos, Energy harvesting from highly unsteady fluid flows using piezoelectric materials, J. Intell. Mater. Syst. Struct. 21 (13) (2010) 1263–1278.

[6] S. Peterson, M. Porfiri, Energy exchange between a vortex ring and an ionic polymer metal composite, Appl. Phys. Lett. 100 (11) (2012) 114102.

[7] A. Bibo, M. Daqaq, Investigation of concurrent energy harvesting from ambient vibrations and wind using a single piezoelectric generator, Appl. Phys. Lett. 102 (24) (2013) 243904.

[8] S. Michelin, O. Doaré, Energy harvesting efficiency of piezoelectric flags in axial flows, J. Fluid Mech. 714 (2013) 489–504.

[9] J. Allen, A. Smits, Energy harvesting eel, J. Fluids Struct. 15 (3-4) (2001) 629–640.

[10] B. Yin, H. Luo, Hydrodynamic interaction of oblique sheets in tandem arrangement, Phys. Fluids 25 (1) (2013) 011902.

[11] A. Erturk, D. Inman, Piezoelectric energy harvesting, John Wiley & Sons, 2011.

[12] O. Goushcha, N. Elvin, Y. Andreopoulos, Interactions of vortices with a flexible beam with applications in fluidic energy harvesting, Appl. Phys. Lett. 104 (2) (2014) 021919.

[13] J. Hu, M. Porfiri, S. Peterson, Energy transfer between a passing vortex ring and a flexible plate in an ideal quiescent fluid, J. Appl. Phys. 118 (11) (2015) 114902.

[14] E. Zivkov, S. Yarusevych, M. Porfiri, S. D. Peterson, Numerical investigation of the interaction of a vortex dipole with a deformable plate, J. Fluids Struct. 58 (2015) 203–215.

[15] E. Zivkov, S. Peterson, S. Yarusevych, Combined experimental and numerical investigation of a vortex dipole interaction with a deformable plate, J. Fluids Struct. 70 (2017) 201–213.

[16] A. Pirnia, J. Hu, S. Peterson, B. Erath, Vortex dynamics and flow-induced vibrations arising from a vortex ring passing tangentially over a flexible plate, J. Appl. Phys. 122 (16) (2017) 164901.

[17] W. X. Huang, S. J. Shin, H. J. Sung, Simulation of flexible filaments in a uniform flow by the immersed boundary method, J. Comput. Phys. 226 (2) (2007) 2206–2228.

[18] W. Weaver Jr, S. Timoshenko, D. Young, Vibration problems in engineering, John Wiley & Sons, 1990.

[19] S. D. Peterson, M. Porfiri, Impact of a vortex dipole with a semi-infinite rigid plate, Phys. Fluids 25 (9) (2013) 093103.

[20] P. Lallemand, L. Luo, Theory of the lattice boltzmann method: Dispersion, dissipation, isotropy, galilean invariance, and stability, Phys. Rev. E 61 (6) (2000) 6546–6562.

[21] D. Yu, R. Mei, W. Shyy, A multi-block lattice boltzmann method for viscous fluid flows, Int. J. Numer. Methods Fluids 39 (2) (2002) 99–120.

[22] X. Zhu, G. He, X. Zhang, Numerical study on hydrodynamic effect of flexibility in a self-propelled plunging foil, Computers & Fluids 97 (2014) 1–20.

[23] S. K. Kang, Immersed boundary methods in the lattice boltzmann equation for flow simulation, Ph.D. thesis, Texas A&M University (2010).

[24] C. Wang, H. Tang, F. Duan, S. Yu, Control of wakes and vortex-induced vibrations of a single circular cylinder using synthetic jets, J. Fluids Struct. 60 (2016) 160–179.

[25] C. Wang, H. Tang, S. Yu, F. Duan, Active control of vortex-induced vibrations of a circular cylinder using windward-suction-leeward-blowing actuation, Phys. Fluids 28 (5) (2016) 053601.

[26] C. Wang, H. Tang, S. Yu, F. Duan, Control of vortex-induced vibration using a pair of synthetic jets: Influence of active lock-on, Phys. Fluids 29 (8) (2017) 083602.

[27] C. Wang, H. Tang, S. Yu, F. Duan, Lock-on of vortex shedding to a pair of synthetic jets with phase difference, Phys. Rev. Fluids 2 (2017) 104701.

[28] C. Wang, H. Tang, Influence of complex driving motion on propulsion performance of a heaving flexible foil, Bioinspir Biomim 14 (1) (2018) 016011.

[29] P. Orlandi, Vortex dipole rebound from a wall, Phys Fluid A: Fluid Dynam 2 (8) (1990) 1429–1436.

[30] G. Carnevale, O. V. Fuentes, P. Orlandi, Inviscid dipole-vortex rebound from a wall or coast, J. Fluid Mech. 351 (1997) 75–103.

[31] J. Wu, H. Ma, M. Zhou, Vorticity and vortex dynamics, Springer Science & Business Media, 2007.

[32] J. Qin, X. Jiang, G. Dong, Z. Guo, Z. Chen, A. Yiannis, Numerical investigation on vortex dipole interacting with concave walls of different curvatures, Fluid Dyn. Res. 50 (4) (2018) 045508.